crystals

Article

Corrosion Behavior and Mechanism of High-Aluminum Inconel 625 in Chlorinated Salts

Ying Wei [1,2,3], Junjia Cao [1,2], Yuehong Zheng [1,2], Haicun Yu [1,2], Penghui Yang [1,2] and Peiqing La [1,2,*]

[1] School of Materials Science and Engineering, Lanzhou University of Technology, Lanzhou 730050, China; lzdtwy@163.com (Y.W.); 13204594308@163.com (J.C.); zhengyuehong1986@126.com (Y.Z.); hcyu@lut.edu.cn (H.Y.); yangph@lut.edu.cn (P.Y.)
[2] State Key Laboratory of Advanced Processing and Recycling of Non-Ferrous Metals, Lanzhou University of Technology, Lanzhou 730050, China
[3] School of Automotive Engineering, Lanzhou Vocational and Technical College, Lanzhou 730070, China
* Correspondence: pala@lut.edu.cn

Abstract: Concentrated solar power plant (CSP) technology holds significant application value in the renewable energy sector for converting solar radiation into thermal and electrical energy. As a heat storage medium for next-generation solar thermal power stations, chloride salts exhibit strong corrosive effects on structural components. To enhance corrosion resistance of the heated body in molten salt environments, Inconel 625 is modified by incorporating aluminum, which facilitates the formation of a protective oxide film. In this study, High-Aluminum Inconel 625, after cold rolling and solution treatment, was immersed in a NaCl-KCl-$MgCl_2$ eutectic chloride melt at 650 °C for 200 h. Post-corrosion analysis revealed the formation of an alumina layer on the surface, effectively mitigating corrosion. Increased aluminum content resulted in thicker alumina layers and the formation of oxidation products, such as Cr_2O_3, Fe_2O_3, MoO_2, and $MgCr_2O_4$ spinel structures, significantly enhancing the alloy's corrosion resistance. The Inconel 625 cold-rolled plate with 5.31 wt% Al exhibited the best corrosion resistance (3510 μm/year), making it a promising candidate for use in next-generation CSP heat storage and exchange components.

Keywords: High-Aluminum Inconel 625; corrosion; chlorinated salts; CSP

Academic Editor: Benilde F. O. Costa

Received: 30 December 2024
Revised: 22 January 2025
Accepted: 26 January 2025
Published: 29 January 2025

Citation: Wei, Y.; Cao, J.; Zheng, Y.; Yu, H.; Yang, P.; La, P. Corrosion Behavior and Mechanism of High-Aluminum Inconel 625 in Chlorinated Salts. *Crystals* **2025**, *15*, 144. https://doi.org/10.3390/cryst15020144

1. Introduction

In order to improve power generation efficiency and reduce costs, chloride salts are considered to be the best heat transfer fluid (HTF) and thermal energy storage (TES) media for the next-generation CSP, and this material can be adapted to operate at temperatures of 800 °C [1,2]. However, due to the aggressive corrosiveness of chlorides and the severe conditions of high-temperature environments, materials, such as molten salt storage tanks, pipes, and heat absorbers, face significant challenges. Inconel 625, a nickel-based superalloy with high concentrations of Ni and Mo, exhibits excellent intergranular corrosion resistance and high-temperature strength [3]. It is widely utilized in high-performance equipment, such as aerospace chemical reactors and pipeline storage tanks. The high strength of Inconel 625 can be attributed to the presence of intermetallic γ'' and Ni_2(Cr,Mo) precipitates, as well as intergranular and intrachrystalline carbides, as reported by Vani Shankar et al. [4] and Yu Cheng et al. [5]. Nevertheless, the corrosion rate of Inconel 625 in chloride molten salts is notably higher compared to other types of salts. Liu et al. [6] examined the corrosion behavior of Inconel 625 at 700 °C in a ternary carbonate mixture (Li_2CO_3-Na_2CO_3-K_2CO_3), revealing a corrosion rate of 936 μm/year after 21 days [7]. Sandia National Laboratories found the corrosion rate of Inconel 625 in solar salt ($NaNO_3$+KNO_3) at 680 °C to be 594 μm/year. In contrast, the corrosion rate of Inconel 625 in a NaCl/LiCl salt environment at 650 °C under inert gas was as high as 2800 μm/year [8]. Additionally, temperature plays a crucial role. Currently, CSP operates at temperatures up to 565 °C, with future developments targeting ultra-high temperatures (700–1000 °C). Judith C et al. reported that the corrosion rate of alloys increases with rising temperatures. Specifically, when the temperature increased from 650 °C to 700 °C, the corrosion rates of Inconel 800H and SS310 more than doubled due to the increased solubility of Cr, Mn, and Fe in the alloy [8,9]. Therefore, it is essential to evaluate whether these alloys can withstand the high-temperature working environments of next-generation CSP systems.

Scholars generally concur that intergranular corrosion represents the predominant form of corrosion. M. Pooja et al. [10] subjected Inconel 625, 310, and 316 stainless steels to sodium hydroxide salts at 700 °C for 48 h. Their findings indicate that Inconel 625 exhibits superior corrosion resistance relative to 310 and 316 stainless steels. Two distinct oxide layers were observed on the surface of the samples, an outer layer of porous NiO and an inner layer of fine-grained Cr_2O_3, attributed to its higher nickel content compared to 310 and 316 stainless steels. Li et al. [11] reported that Alloy 625 experienced corrosion when exposed to nitrates at 565 °C for a period of 15 days. Observations revealed that the oxides formed at pitting sites were enriched in Nb but depleted in Cr and Ni. This indicates that the electrode potential in Nb-rich regions is lower, rendering these areas more susceptible to corrosion. Similarly, Yang et al. [12] also observed that a lower Nb content results in a significant reduction in Laves phase formation, thereby enhancing the alloy's corrosion resistance. Hua Sun et al. [13] investigated the molten salt corrosion behavior of seven nickel-based alloys, including Inconel 625. They discovered that all alloys underwent selective chromium dissolution, resulting in void formation within the matrix. Similarly, Cao et al. [14] examined the corrosion resistance of surface-modified Inconel 625 in an air environment at 750 °C. They found that fine grains and twins formed on the modified alloy's surface. Initially, a thin, chromium-rich protective oxide film developed. However, prolonged exposure led to severe intergranular corrosion, characterized by the complete dissolution of the ultrafine grain layer, thereby diminishing corrosion resistance. This phenomenon is believed to occur because the increased number of ultrafine grains facilitate rapid Cr diffusion. Likewise, Xu et al. [15] demonstrated that chromium dissolution constitutes the primary corrosion mechanism of Inconel 625 in ternary chloride salts. Initially, the corrosion rate was high, but it decreased over time. The formation of MgO and $MgCr_2O_4$ in the corrosion layer played a critical role in mitigating corrosion in air.

In addition, concerning the discussion of the corrosion mechanism, Wang et al. [16] performed a corrosion test on a binary chloride salt mixture of NaCl-KCl (50–50%) at 700 °C. They discovered that the corrosion mechanism of Inconel 625 can be categorized into two stages: at first, electrochemical reactions dominate, followed by active chlorine corrosion in the later stage. Initially, a protective oxide layer, primarily composed of Cr_2O_3, forms on the alloy surface. Subsequently, chloride ions from the molten salt penetrate this Cr_2O_3 layer and interact with metallic elements within the alloy matrix to form metal chlorides. Concurrently, porous oxides are generated, and Cl_2 is released, further compromising the integrity of the protective oxide layer. Ding et al. examined the thermal corrosion behavior of three commercial alloys (SS310, Inconel 800H, and Hastelloy C-276) in chlorinated molten salts under an inert atmosphere at 700 °C for 500 h. Their findings indicated that these alloys failed to meet industrial standards. Specifically, they established a corrosion rate threshold of less than 10 μm/year and a service life of up to 30 years as criteria, proposing a chloride impurity-driven corrosion mechanism [17].

Previous studies have demonstrated that Cr_2O_3 films exhibit limited long-term corrosion resistance in chloride environments, primarily due to intergranular corrosion and continuous chromium dissolution. To address this issue, numerous researchers have investigated methods for enhancing corrosion inhibition. Some studies suggest that applying a protective oxide layer on the alloy surface can improve its corrosion resistance. The thickness and chemical composition of this oxide film are influenced by the material's chemical properties, temperature, and environmental conditions [18,19]. Feng et al. [20] examined the effect of grain size on Inconel 625 films in a NaCl-KCl-$MgCl_2$ environment, finding that larger grain sizes enhance corrosion resistance by reducing Cr depletion. Conversely, Liu et al. reported that Inconel 625 coatings with finer grains exhibited superior corrosion resistance in a 0.5 M NaCl + 0.05 M H_2SO_4 acidic solution [21]. Therefore, the impact of grain size on corrosion resistance remains debatable, as it varies depending on the specific film and corrosive environment. Yu Cheng et al. [5] discovered that the Inconel 625 coating primarily consists of the face-centered cubic (FCC) structured γ-Ni phase, along with Laves and MC phase precipitates present between dendrites. Furthermore, the passivation film formed on the surface was enriched with Cr_2O_3 and MoO_3, which significantly enhanced its corrosion resistance.

Furthermore, several scholars have posited that the Al_2O_3 film exhibits superior corrosion resistance. Aluminum forms a dense protective layer of Al_2O_3 during the reaction process, demonstrating excellent corrosion resistance and stability in molten salt environments [8,22,23]. Roman Savinov et al. [24] found that adding Al and Ti elements to cast Inconel 625 was more likely to form an NB-rich γ' phase. Because the increase in the number and size of γ'' phases is conducive to the resistance of dislocation movement during deformation, the addition of Al and Ti can improve the strength of age-cast Inconel 625. Yang et al. [25] prepared Inconel 625 with an aluminum content of 3 wt% and investigated its corrosion behavior in a 650 °C carbonate melt (Li_2CO_3-Na_2CO_3-K_2CO_3). They observed that the addition of aluminum facilitated the formation of a continuous and dense oxide film (Al_2O_3 + $LiAlO_2$) on the surface, significantly reducing the corrosion rate to 44 µm/year over 48 h and 89 µm/year over 120 h, which is notably lower than previously reported values [6]. Consequently, it is imperative to explore the impact of varying aluminum concentrations on the corrosion mechanisms of molten-salt-exposed Inconel 625. Additionally, the cold rolling process enhances the alloy's resistance to molten salt corrosion by increasing grain boundaries and dislocation defects, thereby impeding the diffusion of corrosive media and promoting the formation of an initial protective oxide layer [26–29]. Therefore, it is necessary to find the best solution to improve the mechanical properties of High-Aluminum Inconel 625 while having better heat resistance and corrosion properties. This study employed a High-Aluminum Inconel 625 sheet with Al content of 5.31 wt% and found that it can achieve a better balance to provide an alternative solution for the next generation of CSP.

2. Materials and Methods

2.1. Preparation of Samples and Salts

The experimental steel was prepared by the research group [30]. High-Aluminum Inconel 625 samples were fabricated through vacuum suspension melting and vacuum arc melting. The compositions are detailed in Table 1. They were heated from room temperature to 1180 °C at a rate of 10 °C/min and then water-quenched after the specified holding time. Following the solution treatment, the plates underwent cold rolling on a two-roll mill to achieve a rolling deformation of 90%, resulting in cold-rolled plates with a final thickness of 0.5 mm. These plates were subjected to a secondary solution treatment for varying durations, as outlined in Table 2. The sheets were cut into specimens measuring

$12 \times 12 \times 0.5$ mm^3. The specimens were ground sequentially using sandpapers of 60#, 240#, 500#, 1000#, 1500#, and 2000# grits, followed by polishing and drying. Subsequently, the polished, cleaned, and dried specimens were placed in alumina crucibles and heated in a muffle furnace from room temperature to 800 °C at a rate of 10 °C/min, held at this temperature for 2 h, and then cooled along with the furnace before proceeding to the next operation.

Table 1. Chemical composition of High-Aluminum Inconel 625 with different Al contents (wt. %).

Alloy No.	Al	Cr	Fe	Nb	Mo	Ni
3Al	3.03	18.05	5.00	4.14	10.02	Balance
5Al	5.31	14.73	5.64	2.64	5.34	Balance
7Al	6.82	10.14	6.27	2.14	6.87	Balance

Table 2. Alloy solution treatment holding time.

Alloy No.	Time
3Al	1 h
5Al	2 h
7Al	6 h

We measured the dimensions and weight of each sample using a vernier caliper and an electronic balance. We selected square alumina crucibles measuring 100 × 50 ×30 mm. Initially, we performed ultrasonic cleaning of the crucibles in distilled water for 10 min, and which were then air dried. We maintained the crucibles at 200 °C for 8 h and then stored them at 70 °C in a drying oven until the experiment commenced. The chlorides utilized in this experiment included sodium chloride, potassium chloride, and magnesium chloride, all sourced from Sinopharm Chemical Reagent and possessing analytical purity. We placed the three salts into separate alumina crucibles and subjected them to a drying process following the sequence 117 °C (24 h) to 180 °C (8 h) to 240 °C (2 h) to 400 °C (1 h) to 600 °C (1 h). We blended the dried salts in the ratio of NaCl-KCl-$MgCl_2$ (24.5 wt.%–20.5 wt.%–55.0 wt.%) [31]. We transferred the mixture into sealed sample bags and stored it in a vacuum drying oven at 70 °C.

2.2. Molten Salt Corrosion Resistance Test

We placed the 3Al, 5Al, and 7Al samples individually into separate crucibles, ensuring that each crucible contained only one type of sample, with four parallel samples for each type. Subsequently, we added the prepared chloride salt to each crucible to ensure that the samples were fully suspended within the molten salt. The crucibles were then sealed and placed in a box resistance furnace (Kewei Yongxing Instrument Co., Ltd., Beijing, China, model SX2-1C-13). No artificial gas was introduced into the furnace chamber. The temperature was increased from ambient conditions to 650 °C at a rate of 5 °C per minute and maintained at this temperature for 200 h. To prevent the evaporation of the molten salt during heating, additional mixed chloride salts were added to the crucibles every 60 h to ensure continuous corrosion of the samples in the molten salt environment.

The corrosion rate was determined using the weight loss method in accordance with ASTM G1-03 [32]. Upon removal of the sample, the surface salt layer was carefully removed using appropriate tools. The sample was then ultrasonically cleaned for 5 min in a solution of distilled water and anhydrous ethanol to ensure thorough cleaning while maintaining the integrity of the metal matrix. To completely remove corrosion products while preserving the metal matrix, a solution of 100 mL of HNO_3 diluted in distilled water to form a total volume of 1000 mL was prepared as per ASTM G1-03 [32] guidelines. This cleaning process was repeated at 1 min intervals until no further mass change was observed. After each cleaning cycle, the sample was dried before reweighing. The number of washes versus the mass loss was plotted (Figure 1), yielding two distinct sections. AB represents the mass loss due to corrosion products, BC represents the mass loss of the underlying metal after corrosion product removal, and point B indicates the total mass loss attributed to corrosion. The corrosion rate was calculated based on the measured mass at point B (Equations (1) and (2)):

$$\Delta \boldsymbol{m} = \boldsymbol{mB} - \boldsymbol{m}_0, \tag{1}$$

$$\boldsymbol{CR}\left(\frac{\mu\text{m}}{\text{year}}\right) = \frac{\boldsymbol{K}\cdot\Delta \boldsymbol{m}/\boldsymbol{S}_0}{\boldsymbol{\rho}\cdot \boldsymbol{t}}, \tag{2}$$

where $\Delta \boldsymbol{m}$ is the quality change of the sample before and after corrosion, g; $\boldsymbol{m_B}$ is the measured mass at point B, g; $\boldsymbol{m}_0$ is the initial weight of the sample, g; $\boldsymbol{K}$ is a constant, taken to be 8.76×10^7; $\boldsymbol{S}_0$ is the initial surface area of the sample, cm^2; $\boldsymbol{\rho}$ is the density of the steel, g/cm^3; and $\boldsymbol{t}$ is the corrosion time of the sample, h.

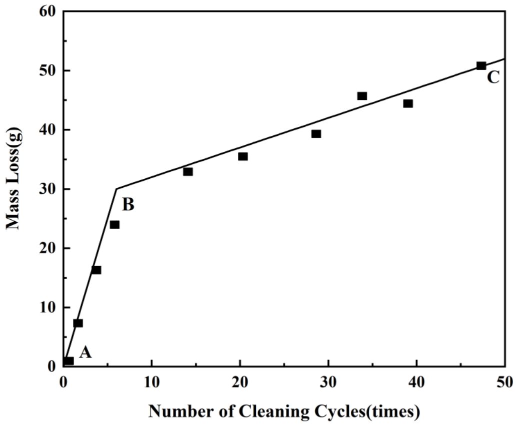

Figure 1. Cleaning cycle and quality loss of corroded specimens [33].

The corrosion rate of the two samples was calculated according to Formulas (1) and (2), respectively, and the average value was taken to eliminate accidental errors.

2.3. Microstructure Characterization

For cross-sectional samples, we embedded them using epoxy resin to prevent the corrosion products from dislodging during the grinding process. We progressively grinded the samples with sandpapers ranging from 120# to 2000# grits, followed by polishing. For surface samples, we removed the surface salt crust using appropriate tools and subsequently cleaned and dried them with distilled water. We analyzed the phase composition of the alloy corrosion products using an X-ray diffraction analyzer (HaoYuan Instrument, Dandong, China, D/Max-2400 type) with Cu Kα radiation, setting the scanning range from 20° to 90° at a scanning speed of 10°/min. We utilized a scanning electron microscope (Thermo Fisher Scientific, Shanghai, China, Axia ChemiSEM) to analyze the corrosion depth and the surface morphology. Additionally, we employed an energy dispersive spectrometer (EDS) to examine the elemental composition and distribution on both the surface and the cross-section of the samples.

3. Results

3.1. Corrosion Rate of High-Aluminum Inconel 625

Figure 2 shows the corrosion bar chart of High-Aluminum Inconel 625. It can be seen that the 5Al sample has the lowest corrosion rate, 3510 μm/y, followed by the 7Al sample, which is similar to 5Al, and the worst is 3Al. Due to the high Ni content in metals, the corrosion rate of nickel-based alloys is generally lower than that of iron-based alloys. The mass loss of 5Al is 197.4 mg, which is not much different from the mass loss of 7Al.

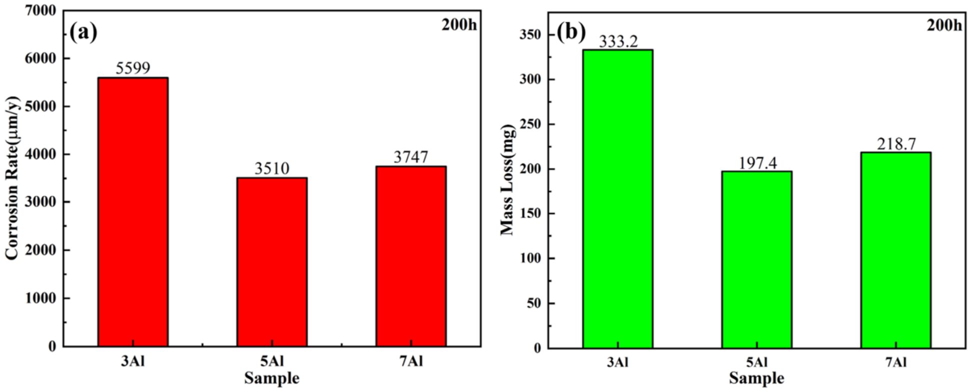

Figure 2. Corrosion bar chart for 200 h. (**a**) Corrosion rate; (**b**) mass loss.

3.2. XRD Phase Analysis

Figure 3 shows the XRD of three High-Aluminum 625 samples with different aluminum additions. It can be seen that the alloy is mainly composed of the γ-phase matrix with a structure of a face-centered cubic (FCC) and a brittle Laves precipitation phase. With the increase in Al content, the intensity of diffraction peak increases. This is consistent with the previous findings of our research group [25,30].

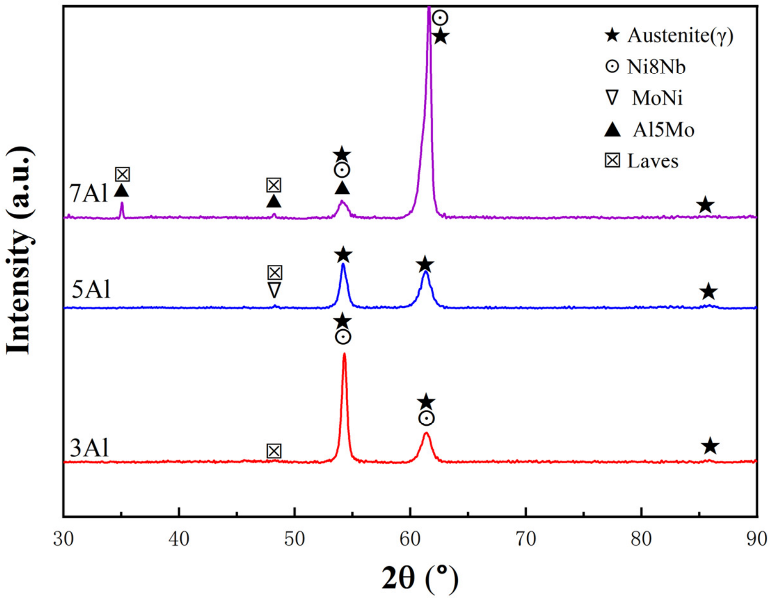

Figure 3. XRD pattern of High-Aluminum Inconel 625 before corrosion: 3Al, 5Al, and 7Al.

Figure 4 shows the XRD patterns of corrosion products of High-Aluminum Inconel 625 with three Al contents. It can be seen that MoO_2 is generated on the surface of the 3Al sample. MoO_2, Cr_2O_3, and $MgCr_2O_4$ corrosion products are formed on the surface of the 5Al sample. Fe_2O_3 and $MgCr_2O_4$ are on the surface of the 7Al sample. By observing the corrosion products, it can be found that the surface of the 5Al sample generates the most corrosion products, while the precipitation of the Cr element reacts with O_2 to form Cr_2O_3 to protect the sample against corrosion.

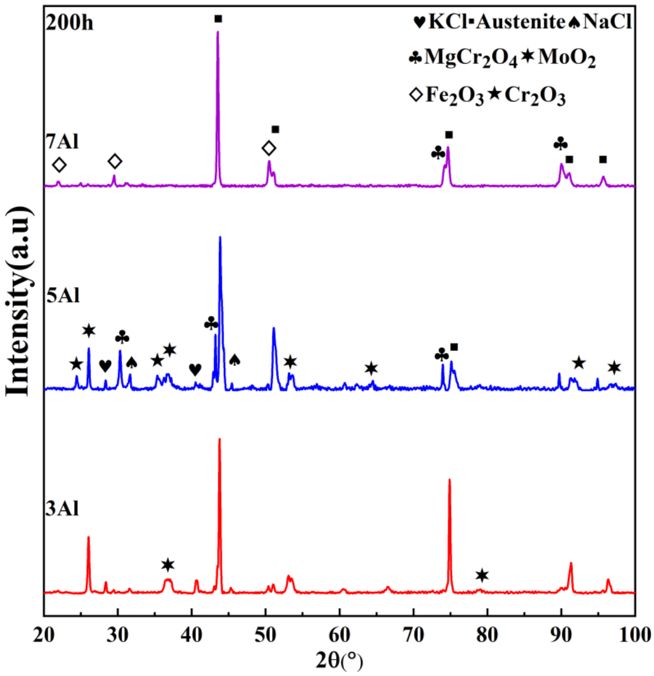

Figure 4. XRD pattern of High-Aluminum Inconel 625 after 200 h of corrosion: 3Al, 5Al, and 7Al.

3.3. Surface Topography Analysis

Figure 5 illustrates the macroscopic morphology of High-Aluminum Inconel 625 samples after 200 h of corrosion. For the 3Al sample, a portion is missing, and the remaining surface appears white. The 5Al sample exhibits salt deposition on its surface, which is uneven and displays gray and black discoloration. The 7Al sample shows salt particles and white or black-gray material adhering to its surface, but it maintains an intact shape.

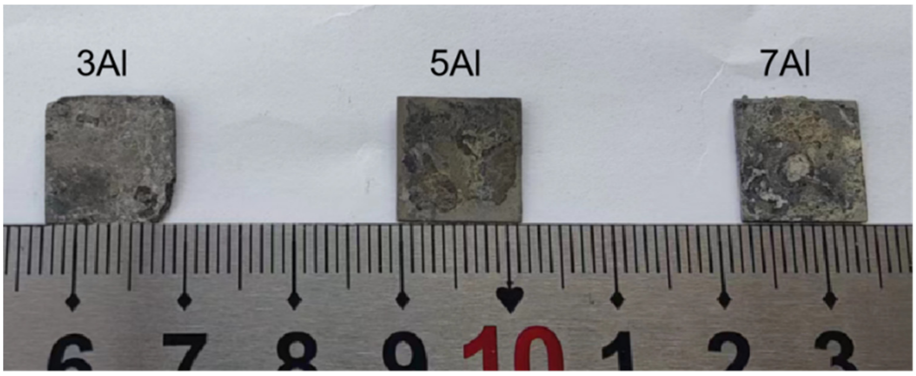

Figure 5. Macroscopic morphology of corrosion samples.

Figure 6 illustrates the SEM surface morphology of the sample following 200 h of 3Al corrosion. A blackened region (labeled as surface feature 2) is evident on the corroded 3Al sample, characterized by corrosion-induced pores. Upon closer inspection of the internal structure, elongated strip-like material (labeled as feature 1) and bulk material (labeled as feature 3) are observable. EDS analysis at features 1, 2, and 3 revealed enrichment of Ni, Mo, and O elements. Additionally, a white, flower-like material (labeled as feature 4) was identified on the surface, primarily composed of Al and O elements, with trace amounts of Cr, Mg, and Ni. Based on atomic percentage analysis (refer to Table 3), the corrosion products were identified as Al_2O_3, $MgCr_2O_4$, and NiO. Further analysis of the bulk white corrosion product (labeled as feature 5) indicated that its primary elemental composition was Ni and O, confirming it to be NiO.

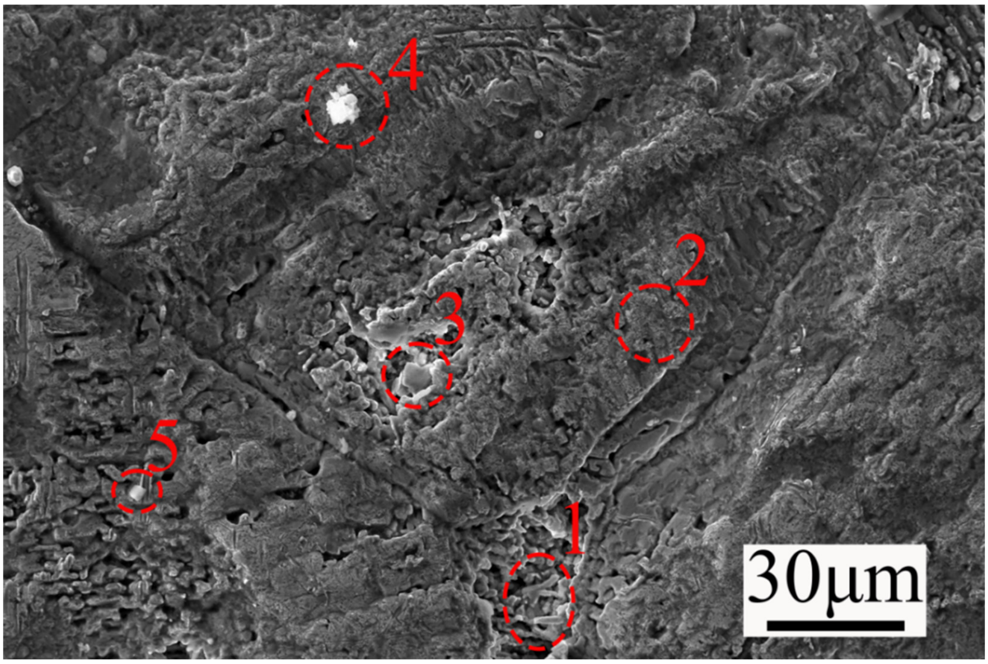

Figure 6. Corrosion surface morphology of 3Al sample.

Table 3. Contents of EDS elements at different locations in Figure 6 (at.%).

Element Content	O	Mg	Al	Cr	Ni	Mo	Fe
1	33.9	1.3	0.5	0.9	50.6	11.7	0.1
2	35.0	1.0	0.5	0.4	48.7	11.4	0.0
3	24.4	3.0	2.3	0.8	58.7	9.6	0.0
4	66.9	2.6	17.8	7.6	3.2	0.9	0.4
5	82.1	0.5	2.3	0.1	10.2	3.5	0.1

Figure 7 illustrates the SEM surface morphology following the corrosion of 5Al. The surface exhibits white granular material (labeled as feature 1) and white, flower-like material (labeled as feature 3). Notably, no corroded pits are observed on the sample's surface. Based on elemental percentage analysis (Table 4), the white bulk corrosion product (labeled as a1) is identified as MgO. EDS dot scan analysis reveals that the white, flower-like corrosion products primarily consist of Mg, O, and Cr elements, leading to the conclusion that these products are $MgCr_2O_4$, supported by atomic percentage and XRD analysis. Additionally, the long black material (labeled as feature 2) contains Ni and O elements, which are identified as NiO through a combination of atomic percentage and XRD analysis.

The surface topography of the 7Al corrosion sample was analyzed as illustrated in Figure 8. Numerous small holes are present on the surface, with granular materials observed within these cavities. Additionally, white massive materials are evident on the surface. EDS analysis of the massive corrosion product (labeled as feature 1) within the cavity revealed that it primarily consists of Mg and O elements, leading to the inference of MgO based on atomic percentage (Table 5). The EDS analysis of the surface region (labeled as feature 2) indicated the presence of Ni, Mo, and O elements. According to the atomic percentage analysis, this layer comprises a metal layer and an NiO layer. EDS analysis of the white massive corrosion product (labeled as feature 3) on the sample surface identified Al and O as the main elements, suggesting the formation of Al_2O_3. Furthermore, EDS analysis of the white massive corrosion product (labeled as feature 4) within the corrosion cavity showed that the primary elements are Mg, Cr, and O. Based on XRD patterns and atomic percentage analysis, the corrosion product is identified as $MgCr_2O_4$

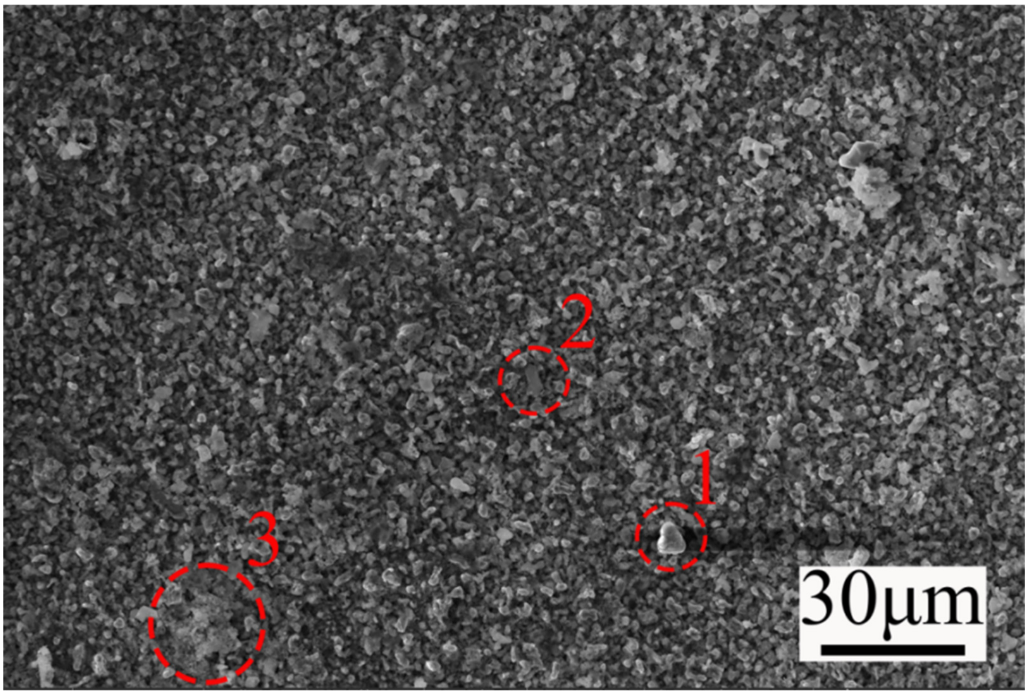

Figure 7. Corrosion surface morphology of 5Al sample (600 times SEM).

Table 4. Contents of EDS elements at different locations in Figure 7 (at.%).

Element Content	O	Mg	Al	Cr	Ni	Mo	Fe
1	51.4	42.9	0.3	0.1	4.9	0.1	0.1
2	66.9	4.3	4.4	0.9	18.2	1.8	0.4
3	53.7	19.0	1.2	14.4	6.6	1.9	0.3

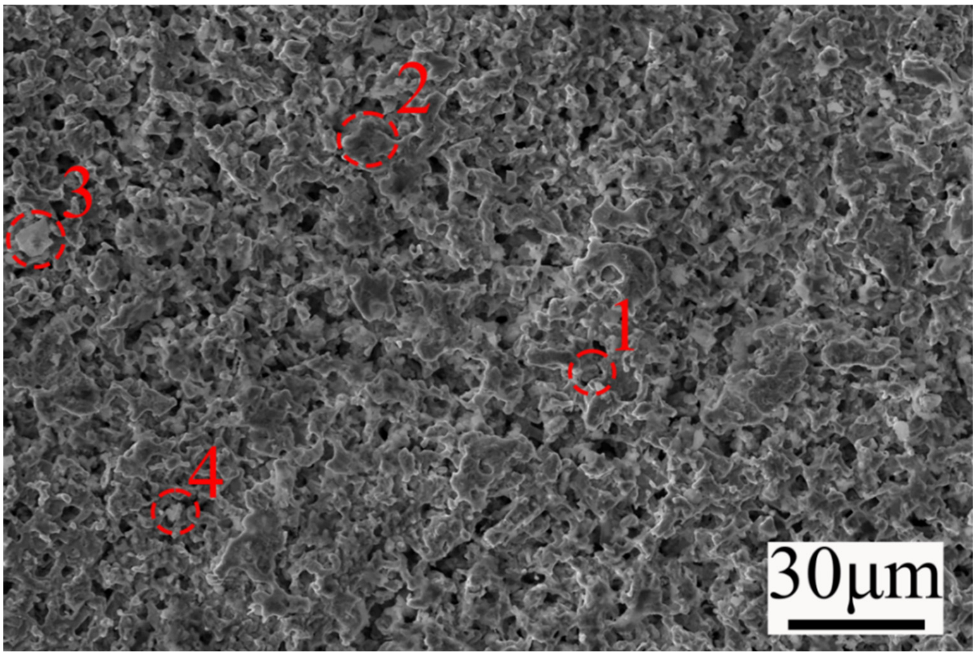

Figure 8. Corrosion surface morphology of 7Al sample.

Table 5. Content of EDS elements at different locations in Figure 8 (at.%).

Element Content	O	Mg	Al	Cr	Ni	Mo
1	46.6	48.0	0.4	0.1	3.7	1.0
2	38.0	0.4	0.2	0.1	48.8	11.5
3	60.4	3.4	29.0	0.3	2.0	2.1
4	57.8	22.8	0.2	11.7	5.2	2.0

3.4. Cross-Section Morphology Analysis and Element Distribution

Cross-sectional analysis of the 3Al samples was conducted, as illustrated in Figure 9. A corrosion layer is observed on the sample surface. Upon magnification, it is evident that the cross-section of the sample consists of two distinct layers, with the upper oxide layer measuring 30 μm in thickness. In the upper region of the matrix layer, there is a notable enrichment of Ni and Mo elements, extending to a depth of 36 μm. Corrosion-induced voids were identified within the matrix. The corrosion layer (labeled as feature 1) primarily comprises Nb and O elements, with atomic percentage analysis confirming the presence of Nb_2O_5. The corrosion layer (labeled as feature 2) was analyzed and found to consist mainly of Cr, Ni, O, and Mg elements. XRD and atomic percentage analysis revealed that the corrosion products are NiO, MgO, and $MgCr_2O_4$. Additionally, black material within the matrix, primarily composed of Ni and O elements, as determined through EDS analysis, was identified as NiO based on atomic percentage analysis (Table 6). Intergranular corrosion was observed, with corrosion progressing inward along grain boundaries, leading to weakened intergranular bonding and reduced mechanical strength of the metal. EDS analysis of the voids within the matrix revealed the presence of NaCl, indicating that chloride salts had penetrated the matrix, facilitating corrosion. This finding confirms the hypothesis that chloride molten salts infiltrated the matrix, displacing matrix elements.

Table 6. Contents of EDS elements at different locations in Figure 9 (at.%).

Element Content	O	Mg	Al	Cr	Ni	Mo	Nb	Cl
1	65.8	7.9	0.0	1.6	0.9	0.0	2.6	0.8
2	59.2	8.4	5.7	10.1	5.7	1.5	5.8	0.8
3	22.5	0.2	0.2	0.4	5.1	0.9	24.2	31.7
4	48.6	2.2	1.7	0.6	24.0	6.3	5.8	5.0

Figure 10 illustrates the SEM cross-sectional morphology of the 5Al alloy after 200 h of corrosion. SEM observations revealed no continuous oxide layer on the surface; instead, numerous small pores were evident both on the sample's surface and within the matrix. Notably, substantial amounts of NaCl and KCl were detected within the matrix layer. EDS surface scanning indicated a slight enrichment of Al and O elements in an approximately 100 μm thick region near the specimen's surface. Additionally, Mg elements were partially present in this corrosion layer. Furthermore, Cr elements were observed within the matrix, while Ni and Mo elements exhibited localized enrichment.

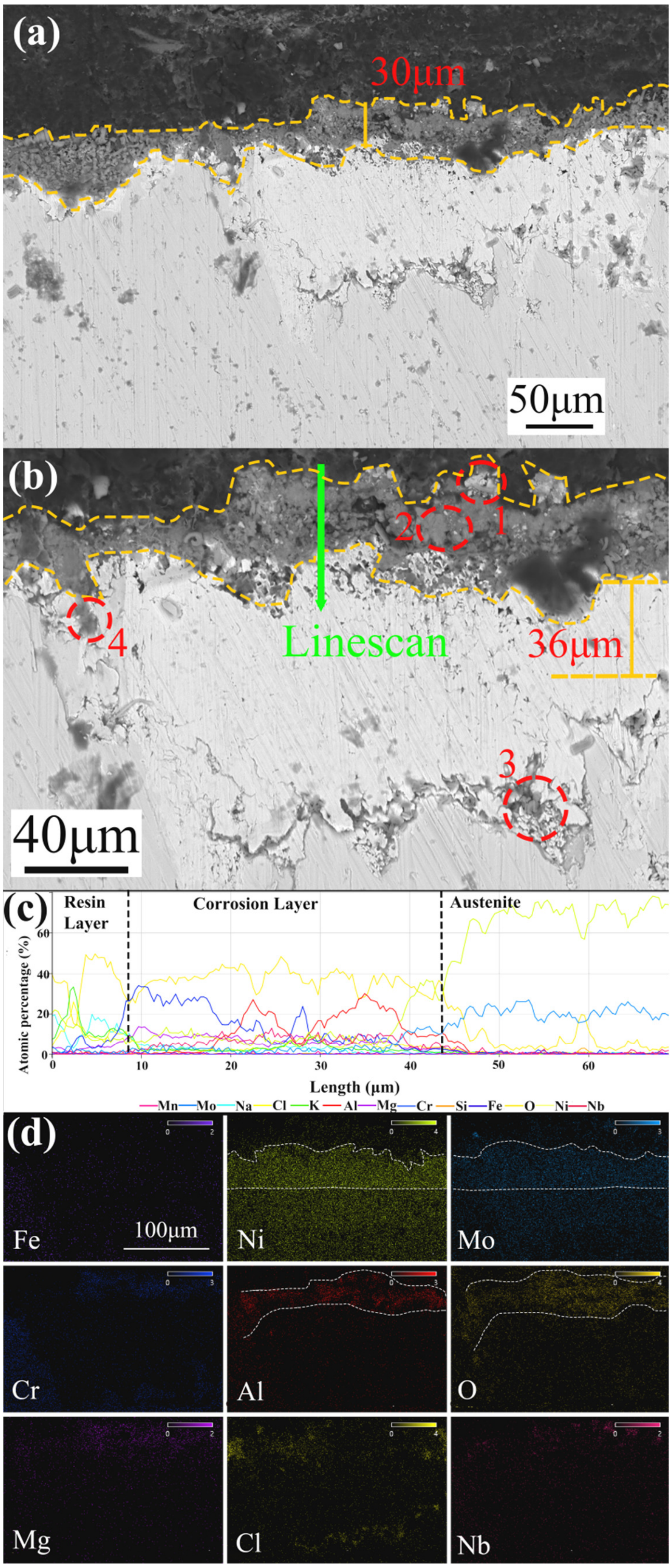

Figure 9. Morphology of corrosion cross-section of 3Al specimen. (**a**) 260× SEM; (**b**) 500× SEM; (**c**) EDS line scanning; (**d**) EDS mapping.

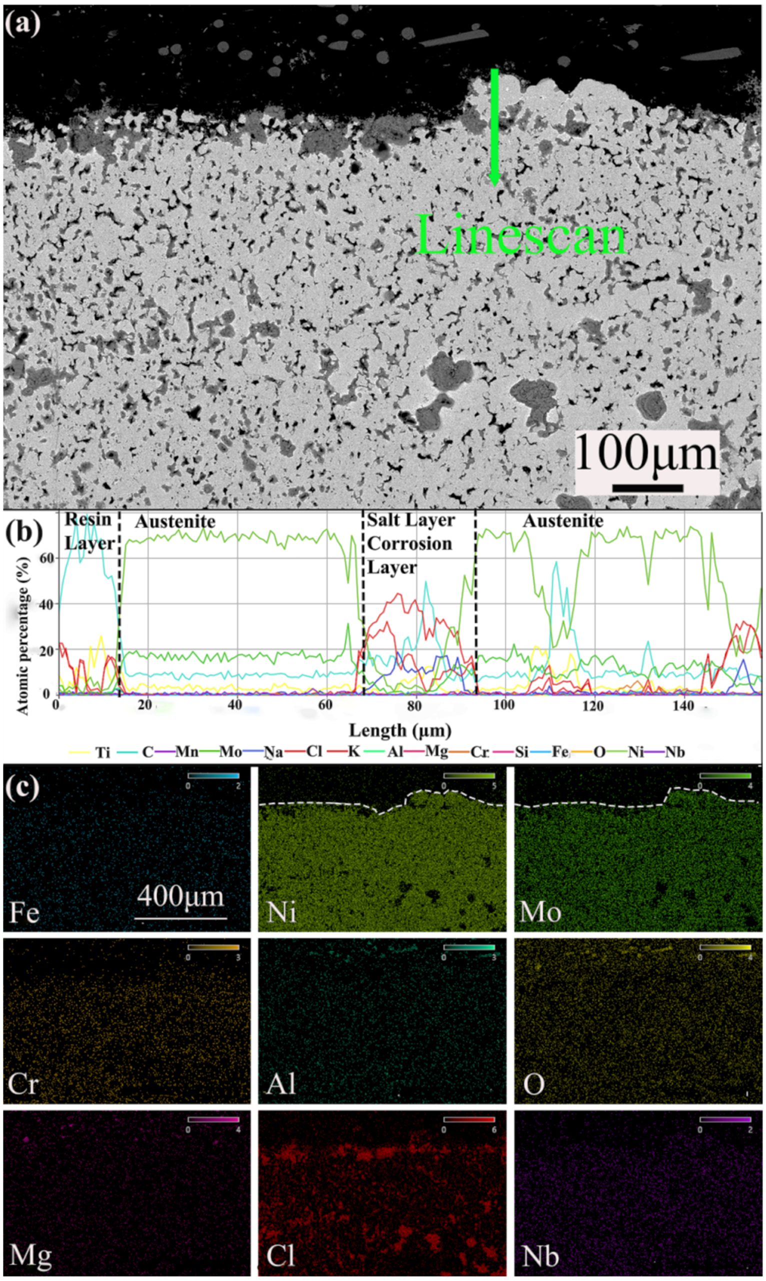

Figure 10. Morphology of corrosion cross-section of 5Al sample. (**a**) SEM; (**b**) EDS line scanning; (**c**) EDS mapping.

Figure 11 illustrates the cross-sectional morphology of the 7Al corrosion sample, revealing a corrosion layer thickness of 42 μm. SEM analysis at high magnification did not reveal any stratification within the corrosion layer. EDS point scanning at various locations provided detailed elemental composition data. Feature 1 primarily contained Na, Cl, and O elements, indicating the presence of NaCl. Feature 2 showed the presence of Na, Cl, Ni, O, and Al elements, with atomic percentage (Table 7) and line scanning analyses confirming the formation of Al_2O_3, NiO, and NaCl. At region 3 above the corrosion layer, the dominant elements were O and Ni, suggesting the formation of NiO. Surface EDS analysis revealed a layer of NaCl enrichment within the sample matrix, indicating that molten salt had penetrated into the sample interior, causing internal corrosion. The observed enrichment of Al and O elements on the surface suggests the formation of an Al_2O_3 layer. However, the non-dense oxide layer indicates partial corrosion damage to the Al_2O_3 during the corrosion process.

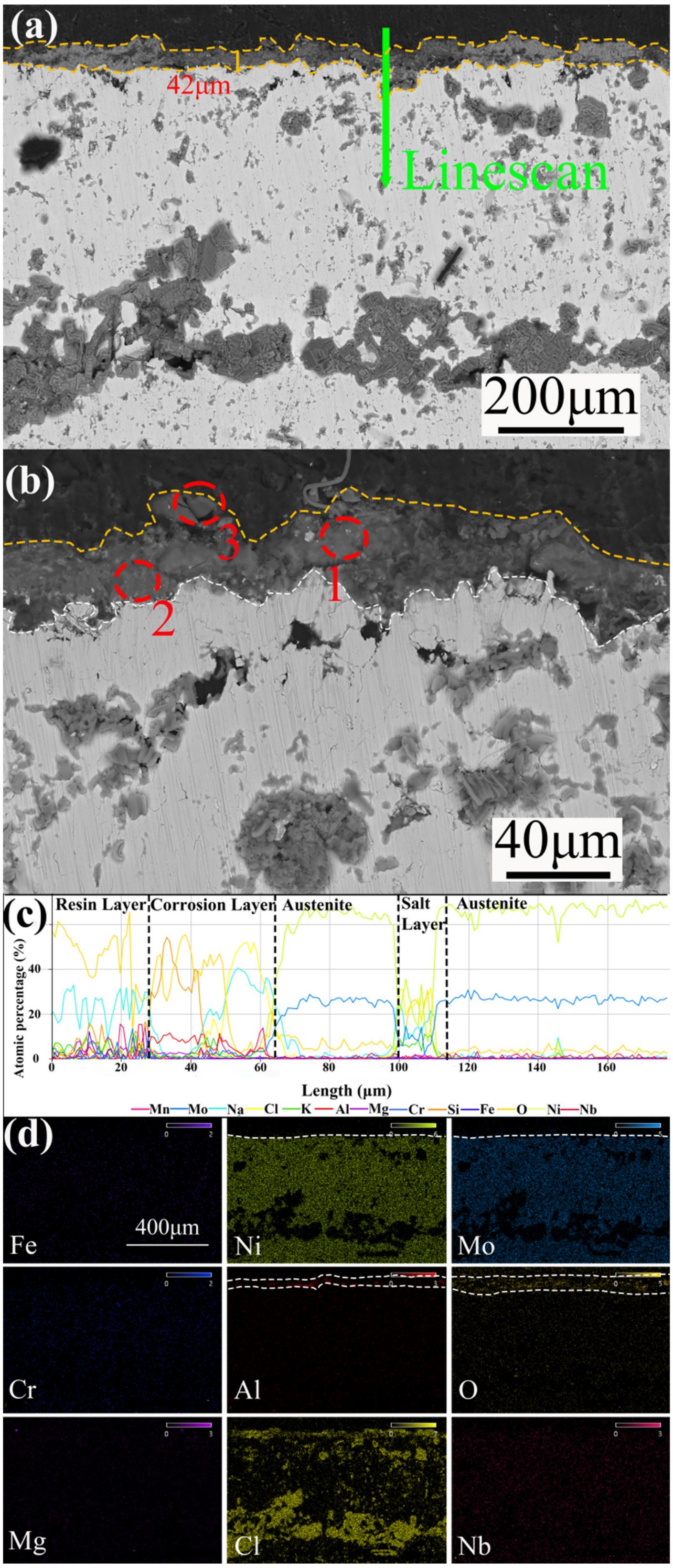

Figure 11. Corrosion cross-section morphology of 7Al sample. (**a**) SEM; (**b**) SEM; (**c**) EDS line scanning; (**d**) 120× EDS mapping.

Table 7. Contents of EDS elements at different locations in Figure 11 (at.%).

Element content	O	Mg	Al	Cr	Ni	Mo	Na	Cl
1	65.8	7.9	0.0	1.6	0.9	0.0	2.6	0.8
2	59.2	8.4	5.7	10.1	5.7	1.5	5.8	0.8
3	48.6	2.2	1.7	0.6	24.0	6.3	5.8	5.0

4. Discussion

4.1. Corrosion Mechanism of High-Aluminum Inconel 625

The corrosion process of In625 alloy in ternary eutectic molten chloride salt is similar to that of 310S [33]. $MgCl_2$ hydrolyzes with high-temperature water vapor in air to produce MgO and HCl gas [34] (Equation (3)).

$$MgCl_2 + H_2O \rightarrow MgO + 2HCl\ (873\ K) = -5.6\ kJ \cdot mol^{-1}, \tag{3}$$

At the same time, $MgCl_2$ itself will undergo a hydrolysis reaction to generate MgOHCl and HCl [35] (Equation (4)).

$$MgCl_2 + H_2O \rightarrow MgOHCl + HCl, \tag{4}$$

At a high temperature of 533–555 °C, MgOHCl is thermally decomposed to form magnesium oxide and hydrochloric acid gas, as shown in Equation (5).

$$MgOHCl \rightarrow MgO + HCl \tag{5}$$

$MgOH^+$ in MgOHCl, as a corrosive impurity, will also affect the corrosion of the alloy. The reaction occurs when MgOHCl is hydrolyzed to produce $MgOH^+$ and Cl^- (Equation (6)), and the free $MgOH^+$ promotes the reaction of MgOHCl with the alloy to produce MgO, metal chloride, and hydrogen (Equation (7)).

$$MgOHCl \rightarrow MgOH^+ + Cl^-, \tag{6}$$

$$xMgOHCl + M \rightarrow xMgO + MCl x + (x/2)H_2\ (M = \text{Alloying element},\ x = 2/3) \tag{7}$$

The O_2 in the air dissolves in the molten chloride salt and diffuses into the metal matrix. Metal alloying elements react with $MgCl_2$ and O_2 to form metal chloride and magnesium oxide [21] (Formula (8)).

$$Cr + 2MgCl_2 + O_2 \rightarrow CrCl_4\uparrow + 2MgO\ (873\ K) = -347.1\ kJ \cdot mol^{-1}, \tag{8}$$

$MgCr_2O_4$ is derived from the interaction between MgO and Cr_2O_3 (Equation (9)).

$$Cr_2O_3 + MgO \rightarrow MgCr_2O_4\ (873\ K) = -37.0\ kJ \cdot mol^{-1}, \tag{9}$$

It has been found [15] that O_2 dissolved in molten chloride salts is converted into reactive oxygen species, which continuously diffuses to metal elements to produce metal oxides, such as Cr_2O_3 and Fe_2O_3. However, Cr_2O_3 and Fe_2O_3 are only intermediate products, and Cr_2O_3 reacts with FeO and NiO to produce $FeCr_2O_4$ and $NiCr_2O_4$. At the same time, Fe_2O_3 and NiO react to form $NiFe_2O_4$ (Equations (10)–(12)).

$$Cr_2O_3 + FeO \rightarrow FeCr_2O_4, \tag{10}$$

$$Cr_2O_3 + NiO \rightarrow NiCr_2O_4, \tag{11}$$

$$Fe_2O_3 + NiO \rightarrow NiFe_2O_4, \tag{12}$$

According to previous research, it has been established that the corrosion of metals in iron-based alloys is significantly influenced by the presence of chromium (Cr). And, it has also been observed in nickel-based alloys. The dissolution of Cr can be attributed to two primary factors, including, firstly, the heterogeneous distribution of elements within the alloy matrix. Secondly, under high-temperature conditions, Cr exhibits rapid diffusion and migration, leading to its increased reactivity with corrosion products [36]. When oxygen (O_2) and water (H_2O) are dissolved in molten chloride salts, Cr readily participates in the ensuing reactions, as described by the following equations (Equations (13)–(18)):

$$H_2O + 2Cl^- \rightarrow O^{2-} + 2HCl, \tag{13}$$

$$4Cl^- + O_2 \rightarrow 2O^{2-} + 2Cl_2, \tag{14}$$

$$Cr + 2Cl_2 \rightarrow CrCl_4, \tag{15}$$

$$2CrCl_4 + 4MgO \rightarrow MgCr_2O_4 + 3MgCl_2 + Cl_2\ (873\ K) = -39.6\ kJ \cdot mol^{-1}, \tag{16}$$

$$2CrCl_4 + 3O^{2-} \rightarrow Cr_2O_3 + 6Cl^- + Cl_2, \tag{17}$$

$$2Cr_2O_3 + 4O^{2-} + 3O_2 \rightarrow 4CrO_2{}^{-4}, \tag{18}$$

Therefore, chromium not only contributed to the formation of Cr_2O_3, $MgCr_2O_4$, and $CrCl_4$ but also substituted for elements in the molten salt. During this substitution process, micro-porous structures were generated, serving as channels that led to an irregular morphology on the surface of the sample.

4.2. Influence of Different Aluminum Contents on the Corrosion Resistance of High-Aluminum Inconel 625

The incorporation of alloying elements significantly enhances the properties of nickel-based alloys. Specifically, increasing the aluminum content not only improves the strength and hardness but also promotes the formation of a dense and stable oxide film, thereby enhancing oxidation and corrosion resistance. Al_2O_3 forms on the surface of three High-Aluminum Inconel 625 samples with varying aluminum contents; however, the corrosion products differ among these samples. In the 3Al sample, Ni and Mo elements are enriched in the upper layer, indicating that active oxygen species within the matrix have reacted with these elements. This enrichment inevitably leads to a depletion or reduction of elements within the matrix. According to the law of conservation of matter, molten salt infiltrates the depleted areas, intensifying corrosion. The 5Al sample exhibits the most abundant corrosion products, suggesting that its protective layer is less prone to falling off and dissolving in molten salt compared to the other two samples. Previous studies indicate that MgO and $MgCr_2O_4$ oxide layers can protect metals from molten salt corrosion and reduce weight loss after corrosion. Fe_2O_3 was detected on the surface of the 7Al sample, indicating that Fe elements precipitated to form a protective layer, slowing down corrosion. Comparing the three samples with different Al contents reveals that Al content does not affect the formation of $MgCr_2O_4$ and Cr_2O_3. The Al_2O_3 oxide layer in the 7Al sample is approximately 6 μm thicker than in the 3Al sample. Compared to the 7Al sample, a MoO_2 oxide layer was observed in the 5Al sample. The varying aluminum content influences the types of corrosion products, as different levels of aluminum lead to variations in the thickness of the Al_2O_3 oxide layer. A thicker oxide layer inhibits the formation of other protective oxides.

5. Conclusions

In this paper, the corrosion behavior of High-Aluminum Inconel 625 was investigated at 650 °C after exposure to a molten terpolymer eutectic chloride salt. The corrosion rate of the samples after 200 h of corrosion was determined using the weight loss method. Surface and cross-sectional characterization of the corrosion layer was conducted, and the corrosion mechanism of the nickel-based alloy in chloride molten salts was examined. Additionally, the influence of different aluminum contents on the corrosion resistance of the samples was evaluated. The key findings are summarized as follows:

(1) The corrosion mechanism of nickel-based alloys in ternary eutectic chloride molten salts can be elucidated from two perspectives: impurity-induced corrosion and the oxidation–chlorination of alloy components. Firstly, $MgCl_2$ undergoes hydrolysis and chemical reactions, producing corrosive byproducts, such as Mg (OH)+ and HCl gas, which exacerbate the corrosion process. Secondly, during the corrosion of Alloy 625, the matrix metal elements (Cr, Fe, Ni, Mo, etc.) undergo continuous oxidation and chlorination. Notably, Cr plays a predominant role in the corrosion process within chloride molten salts, manifesting as intergranular corrosion and selective dissolution of Cr. This corrosion propagates inward along grain boundaries, weakening intergranular bonding and allowing chloride salts to penetrate into the matrix, corroding pores and displacing alloy elements.

(2) In an experimental study on the corrosion behavior of High-Aluminum Inconel 625, it was observed that the corrosion rate was lowest for the 5Al alloy at 3510 μm/year. A protective Al_2O_3 oxide layer formed on the alloy surface, effectively mitigating corrosion. Specifically, the corrosion layer thickness for the sample containing 3.03 wt% Al was 30 μm, while that for the sample with 6.82 wt% Al was 42 μm. In addition, the 5Al sample exhibits the most abundant corrosion products, and the formation of corrosion products, such as $MgCr_2O_4$ Cr_2O_3, and MoO_2, also effectively slowed down the corrosion.

Author Contributions: Conceptualization, Y.W. and P.L.; methodology, Y.W. and J.C.; software, H.Y. and Y.Z.; validation, P.L.; formal analysis, Y.W. and J.C.; investigation, Y.Z.; resources, Y.W.; data curation, Y.Z. and P.Y.; writing—original draft preparation, J.C.; writing—review and editing, Y.W.; visualization, P.Y.; supervision, P.L.; project administration, H.Y.; funding acquisition, P.L. All authors have read and agreed to the published version of the manuscript.

Funding: This research was funded by Yuehong Zheng, Peiqing La, and Lanzhou Vocational Technical College, "Foundation of Key Laboratory of Solar Power System" (Grant No. 2024SPKL02), and "2024 College-level Scientific Research Project of Lanzhou Vocational Technical College" (Grant No. 2024XY-26).

Data Availability Statement: The data presented in this study are available upon request from the corresponding author.

Conflicts of Interest: All authors have read and agreed to the published version of the manuscript. The authors declare no conflicts of interest. The sponsors participate in the specific work of the research but do not influence the submission of the manuscript.

References

1. Villada, C.; Ding, W.; Bonk, A.; Bauer, T. Engineering molten $MgCl_2{}^{-}KCl^{-}NaCl$ salt for high-temperature thermal energy storage: Review on salt properties and corrosion control strategies. *Sol. Energy Mater. Sol. Cells* **2021**, *232*, 111344. [CrossRef]
2. Gauché, P.; Rudman, J.; Mabaso, M.; Willem; Landman, W.A.; von Backström, T.W.; Brent, A.C. System value and progress of CSP. *Sol. Energy* **2017**, *152*, 106–139. [CrossRef]
3. Singh, J.B. Corrosion Behavior of Alloy 625. In *Alloy 625. Materials Horizons: From Nature to Nanomaterials*; Springer: Singapore, 2022. [CrossRef]

4. Shankar, V.; Rao, K.B.S.; Mannan, S.L. Microstructure and mechanical properties of Inconel 625 superalloy. *J. Nucl. Mater.* **2001**, *288*, 222–232. [CrossRef]
5. Cheng, Y.; Sun, Y.; Zhang, S.; Cheng, W.; Xu, Y.; Wei, S.; Luo, J. Corrosion and wear resistance of inconel 625 and inconel 718 laser claddings on 45 steel. *J. Alloys Compd.* **2025**, *1013*, 178368. [CrossRef]
6. Liu, T.; Xu, X.; Liu, W.; Zhuang, X. Corrosion of alloys in high temperature moltensalt heat transfer fluids with air as the cover gas. *Sol. Energy* **2019**, *191*, 435–448. [CrossRef]
7. Kruizenga, A.M.; Gill, D.D.; LaFord, M.E. *Corrosion of High Temperature Alloys in Solar Salt at 400, 500, and 680 °C*; Sandia National Lab: Livermore, CA, USA, 2013.
8. Gomez-Vidal, J.C.; Tirawat, R. Corrosion of alloys in a chloride molten salt (NaCl-LiCl) for solar thermal technologies. *Sol. Energy Mater. Sol. Cells* **2016**, *157*, 234–244. [CrossRef]
9. Luo, J.; Deng, C.K.; Li, N.; Han, R.F.; Liu, H.H.; Wang, J.Q.; Cui, X.Y.; Xiong, T.Y. Corrosion behavior of SS316L in ternary Li_2CO_3–Na_2CO_3–K_2CO_3 eutectic mixture salt for concentrated solar power plants. *Sol. Energy Mater. Sol. Cells* **2020**, *217*, 110679. [CrossRef]
10. Pooja, M.; Ravishankar, K.S.; Madav, V. High temperature corrosion behaviour of stainless steels and Inconel 625 in hydroxide salt. *Mater. Today Proc.* **2021**, *46*, 2612–2615. [CrossRef]
11. Li, N.; Tariq, N.u.H.; Han, B.; He, R.; Wang, J.; Cui, X.; Xiong, T. Study of Corrosion Performance and Mechanisms of P91, 304SS and IN625 Alloys in Molten Nitrate Salts Used for Thermal Energy Storage System. *Metals* **2023**, *13*, 806. [CrossRef]
12. Yang, P.; Du, L.; Wang, R.; La, P.; Guo, T. Review of the Current Status of Domestic and International Research on Inconel 625 Alloy. *Foundry Technol.* **2023**, *04*, 44. [CrossRef]
13. Sun, H.; Wang, J.; Li, Z.; Zhang, P.; Su, X. Corrosion behavior of 316SS and Ni-based alloys in a ternary NaCl-KCl-$MgCl_2$ molten salt. *Sol. Energy* **2018**, *171*, 320–329. [CrossRef]
14. Gao, B.; Yu, R.; Chen, S.; Hu, H.; Wu, K.; Zhang, X. Corrosion behavior of surface-modified Ni-based alloys in molten NaCl–KCl for thermal energy storage. *Mater. Chem. Phys.* **2025**, *332*, 130288. [CrossRef]
15. Xu, Z.; Guan, B.; Wei, X.; Lu, J.; Ding, J.; Wang, W. High-temperature corrosion behavior of Inconel 625 alloy in a ternary molten salt of NaCl-$CaCl_2$-$MgCl_2$ in air and N_2. *Sol. Energy* **2022**, *238*, 216–225. [CrossRef]
16. Wang, X.; Liu, Z.; Cheng, K.; Shen, Y.; Li, J. Corrosion characteristics of Inconel 625 cladding layer and NiCrMoAl cladding layer in molten NaCl-KCl and NaCl-KCl-Na_2SO_4. *Corros. Sci.* **2023**, *221*, 111308. [CrossRef]
17. Ding, W.; Shi, H.; Xiu, Y.; Bonk, A.; Weisenburger, A.; Jianu, A.; Bauer, T. Hot corrosion behavior of commercial alloys in thermal energy storage material of molten $MgCl_2$/KCl/NaCl under inert atmosphere. *Sol. Energy Mater. Sol. Cells* **2018**, *184*, 22–30. [CrossRef]
18. Sarvghad, M.; Maher, S.D.; Collard, D.; Tassan, M.; Will, G.; Steinberg, T.A. Materials compatibility for the next generation of Concentrated Solar Power plants. *Energy Storage Mater.* **2018**, *14*, 179–198. [CrossRef]
19. Chen, H.Z.; Li, B.R.; Wen, B.; Ye, Q.; Zhang, N.Q. Corrosion behaviours of iron-chromium-aluminium steel near the melting point of various eutectic salts. *Sol. Energy Mater. Sol. Cells* **2020**, *210*, 110510. [CrossRef]
20. Feng, J.; Mao, L.; Yuan, G.; Zhao, Y.; Vidal, J.; Liu, L.E. Grain size effect on corrosion behavior of Inconel 625 film against molten $MgCl_2$-NaCl-KCl salt. *Corros. Sci.* **2022**, *197*, 110097. [CrossRef]
21. Liu, B.; Wei, X.; Wang, W.; Lu, J.; Ding, J. Corrosion behavior of Ni-based alloys in molten NaCl-$CaCl_2$-$MgCl_2$ eutectic salt for concentrating solar power. *Sol. Energy Mater. Sol. Cells* **2017**, *170*, 77–86. [CrossRef]
22. Lantelme, F.; Groult, H. *Molten Salts Chemistry: From Lab to Applications*; Elsevier: Amsterdam, The Netherlands, 2013.
23. Vignarooban, K.; Xu, X.; Arvay, A.; Hsu, K.; Kannan, A.M. Heat transfer fluids for concentrating solar power systems–A review. *Appl. Energy* **2015**, *146*, 383–396. [CrossRef]
24. Savinov, R.; Wang, Y.; Shi, J. Evaluation of microstructure, mechanical properties, and corrosion resistance for Ti-doped inconel 625 alloy produced by laser directed energy deposition. *Mater. Sci. Eng. A* **2023**, *884*, 145542. [CrossRef]
25. Yang, P.; Cao, R.; Wang, R.; Jia, H.; Li, C.; Li, Z.; Wang, Y.; La, P. Investigation of the high temperature molten salt corrosion properties of Inconel625 alloy with Al. *Mater. Charact.* **2024**, *217*, 114397. [CrossRef]
26. Gao, Q.; Jiang, Y.; Liu, Z.; Zhang, H.; Jiang, C.; Zhang, X.; Li, H. Effects of alloying elements on microstructure and mechanical properties of Co–Ni–Al–Ti superalloy. *Mater. Sci. Eng. A* **2020**, *779*, 139139. [CrossRef]
27. Dong, H.; Ye, Z.; Wang, P.; Li, D.; Zhang, Y.; Li, Y. Effect of cold rolling on the oxidation resistance of T91 steel in oxygen-saturated stagnant liquid lead-bismuth eutectic at 450 °C and 550 °C. *J. Nucl. Mater.* **2016**, *476*, 213–217. [CrossRef]
28. Naraparaju, R.; Christ, H.J.; Renner, F.U.; Kostka, A. Effect of shot-peening on the oxidation behaviour of boiler steels. *Oxid. Met.* **2011**, *76*, 233–245. [CrossRef]
29. Wang, Z.B.; Tao, N.R.; Tong, W.P.; Lu, J.; Lu, K. Diffusion of chromium in nanocrystalline iron produced by means of surface mechanical attrition treatment. *Acta Mater.* **2003**, *51*, 4319–4329. [CrossRef]
30. Du, L.L. Design and preparation of high temperature resistant molten salt high alumina 625 alloy and its properties. *Lanzhou Univ. Technol.* **2023**, 9–17. (In Chinese)

31. Mortazavi, A.; Zhao, Y.; Esmaily, M.; Allanore, A.; Vidal, J.; Birbilis, N. High-temperature corrosion of a nickel-based alloy in a molten chloride environment–The effect of thermal and chemical purifications. *Sol. Energy Mater. Sol. Cells* **2022**, *236*, 111542. [CrossRef]
32. *ASTM G1-03*; e1 Standard Practice for Preparing, Cleaning, and Evaluating Corrosion Test Specimens. ASTM International: West Conshohocken, PA, USA, 2017.
33. Wei, Y.; Cao, J.; Yu, H.; Sheng, J.; La, P. Effect of Mg Addition on Molten Chloride Salt Corrosion Resistance of 310S Stainless Steel with Aluminum. *Metals* **2024**, *14*, 1109. [CrossRef]
34. Ding, W.; Shi, H.; Jianu, A.; Xiu, Y.; Bonk, A.; Weisenburger, A.; Bauer, T. Molten chloride salts for next generation concentrated solar power plants: Mitigation strategies against corrosion of structural materials. *Sol. Energy Mater. Sol. Cells* **2019**, *193*, 298–313. [CrossRef]
35. Zhao, Y.; Klammer, N.; Vidal, J. Purification strategy and effect of impurities on corrosivity of dehydrated carnallite for thermal solar applications. *RSC Adv.* **2019**, *9*, 41664–41671. [CrossRef]
36. Qiu, J.; Zou, Y.; Yu, G.; Liu, H.; Jia, Y.; Li, Z.; Huai, P.; Zhou, X.; Xu, H. Compatibility of container materials with Cr in molten FLiNaK salt. *J. Fluor. Chem.* **2014**, *168*, 69–74. [CrossRef]